Materials and Design 52 (2013) 556–564

Contents lists available at SciVerse ScienceDirect

Materials and Design

journal homepage: www.elsevier.com/locate/matdes

Technical Report

Analysis of heat input effect on the mechanical properties of Al-6061-T6 alloy weld joints

Javier A. Vargas, Jaime E. Torres, Jovanny A. Pacheco, Roque J. Hernandez *

Department of Mechanical Engineering, Materials, Processes and Design Research Group, Universidad del Norte, Barranquilla, Colombia

ARTICLE INFO

Article history:
Received 28 November 2012
Accepted 25 May 2013
Available online 7 June 2013

ABSTRACT

Plates of AA6061-T6 with 4.8 mm of thickness were welded with an ER4043 electrode (1.19 mm in diameter) using the typical simple butt joint to investigate the effect on the mechanical properties of aluminum alloy 6061-T6 due to the Gas Metal Arc Welding (GMAW) process. The parameters involved in the welding process were related to the variation of the yield strength and microhardness. A transient thermal analysis was developed to model the problem in a numerical form using Finite Element Method (FEM) and these results were compared with experimental data showing good agreement. It was observed that the amount of energy absorbed by the base material determines the maximum temperatures reached by the aluminum and microstructural changes produced by high metal temperatures, significantly influence the properties of the alloy. For a case with 120 A, 18.0 V and 5.26 mm/s in travel speed, the reduction of yield strength was 45.1% and for Vickers microhardness was 45.2%. For another case with 140 A, 20.5 V and 5.36 mm/s in travel speed, the reductions were 40.9% and 38.4% for yield strength and Vickers microhardness respectively. The transformation of precipitates β'' in β' and β explain these changes.

© 2013 Elsevier Ltd. All rights reserved.

1. Introduction

The effect of heat generated by the Gas Metal Arc Welding (GMAW) process on AA6061-T6 alloy has been widely studied in the literature. Investigations about the influence of the grain size in the weld heat-affected zone had been considered [1]. In addition, the effect of heat input using the hardness profiles was analyzed [2] and also the heat effect via the evolution of precipitates [3]. GMAW is one of the most used joining techniques and the heat generated by this welding process has been studied for several aluminum alloys (series 6000, 7000 and 8000). The GMAW process had been described by several authors [3–5]; thus different aspects of the process are being studied, including the residual stress [6,7], overthickness, porosity, cracking and the degree of involvement of heat resistance. Most recently, the influence on the microstructure and strength due to interactions between different groups of particles that form at various temperatures was studied [8]. According to [9] the ultimate strength significantly reduces to more than 50% with respect to the base material. An analysis of the mechanical strength for Al-6061-T6 and its microstructure, for different types of welding joints [10] and also a study for the local mechanical properties using micro-traction and instrumented indentation [11] has been developed. Also the influence of welding parameters on fatigue life has been studied by [12].

However, only one reference quantified the reduction on the mechanical properties based on the ultimate strength [9] even when in most design applications the failure criteria is related to the yield strength. Therefore, the purpose of this research is to characterize the mechanical behavior of the welded joint using the yield strength and the microhardness. The approach employed to analyze this problem would be a practical tool to design welding processes and predict the final properties of a mechanical welded component. Several works have been developed in the correlation among process variables, microstructure and mechanical properties [13–15]. This article focuses on the effect of heat input on mechanical properties such as yield strength and microhardness and its relationship with GMAW process parameters such as travel speed, current intensity and voltage as shown in Fig. 1. A numerical model for the thermal analysis was generated and implemented computationally and the results were validated with experimental data. Transmission Electron Microscopy (TEM) and Differential Scanning Calorimetry (DSC) were used to characterize the evolution of hardening precipitates β'', β' and β and the intermetallic compound Mg_2Si.

2. Proposed thermal model

To model this thermal process, the heat absorbed by welded sheets has to be calculated. In this analysis radiation and convection losses are considered. Other losses are not taken into account because their magnitudes are not significant. Eq. (1) describes the

* Corresponding author. Tel.: +57 5 3509272; fax: +57 5 3509255.
E-mail address: roqherna@uninorte.edu.co (R.J. Hernandez).

0261-3069/$ - see front matter © 2013 Elsevier Ltd. All rights reserved.
http://dx.doi.org/10.1016/j.matdes.2013.05.081

Nomenclature

C_p	fluid heat capacity (W s/kg °C)	Q	heat input (W/m^2)
g	acceleration due to earth's gravity (m/s^2)	σ	Stefan–Boltzmann constant (W/(m^2 K^4))
Gr_L	Grashof number	S_u	ultimate tensile strength (MPa)
h_m	mean convective heat transfer coefficient (W/m^2 °C)	S_y	yield tensile strength (MPa)
HV	Vickers hardness	T_∞	bulk temperature (°C)
I	current (A)	T_s	surface temperature (°C)
k	thermal conductivity (W/m^2 °C)	v	voltage (V)
L	characteristic length (avg. length) (m)	ρ	density (kg/m^3)
Nu_m	mean Nusselt number	υ	kinematic viscosity (m^2/s)
Pr	Prandtl number	ε	emissivity

radiation losses that mainly occur in the weld area (higher temperature) [16]. And this equation assumes no interaction between adjacent surfaces and the hot surface.

$$q_{rad} = \varepsilon\sigma(T_s^4 - T_\infty^4) \tag{1}$$

Applying Eq. (1) for the aluminum: In the hottest area, the value for q_{rad} is 1640 W/m^2; for an average temperature zone of 150 °C then q_{rad} is 53 W/m^2. Table 1 lists the thermal properties for the AA6061-T6 required in the analysis [17].

The following expressions from [18,19] correlates Nusselt, Grashof and Prandtl numbers with mean convective heat transfer coefficient. For a horizontal plate:

$$Nu_m = c \cdot (Gr_L Pr)^n \tag{2}$$

$$Nu_m = \frac{h_m L}{k} \tag{3}$$

$$Gr_L = \frac{g\beta(T_s - T_\infty)L^3}{\upsilon^2} \tag{4}$$

where β is the volumetric thermal expansion coefficient (approximately $1/T$, where T is the absolute temperature for ideal fluids).

The values of c and n coefficients depend on the regime and the location of the surface; Table 2 shows them. Table 3 presents the properties of the atmospheric air at different temperatures. Table 4 summarizes the results for different temperatures applying Eqs. (2)–(4). Considering that approximately 80% of the plate remains significantly below the maximum temperature, weighted values

Table 1
AA6061-T6 properties.

Property	Value
$\varepsilon_{\text{polished aluminum}}$	$\varepsilon_{Al} = 0.04$
Density (ρ)	$\rho = 2.7$ gr/cm^3
Coefficient of linear thermal expansion (α)	23.6 μm/m K
Fluid heat capacity at 20 °C (C_p)	896 J/kg
Liquidus temperature (T_{liq})	652 °C
Solidus temperature (T_{sol})	582 °C
Thermal conductivity (k)	$k = 167$ W/m K

Table 2
Values of c and n coefficients for different regimes in free convection. Obtained from [18].

Type of flow	Plate orientation	$Gr_L \cdot Pr$ range	c	n
Turbulent	Face up	$[2 \times 10^7 – 3 \times 10^{10}]$	0.14	1/3
Turbulent	Face up	$[10^5 – 2 \times 10^7]$	0.54	¼
Laminar	Face down	$[3 \times 10^5 – 3 \times 10^{10}]$	0.27	¼

Table 3
Properties of the atmospheric air at 30 and 340 °C. Obtained from [18].

	$T = 30$ °C	$T = 340$ °C
C_p (W s/kg °C)	1.06	1.025
k (W/m °C)	0.0273	0.0366
ρ (kg/m^3)	1.371	0.8108
υ (m^2/s)	0.1664×104	0.3018×10^4
Pr	0.703	0.686

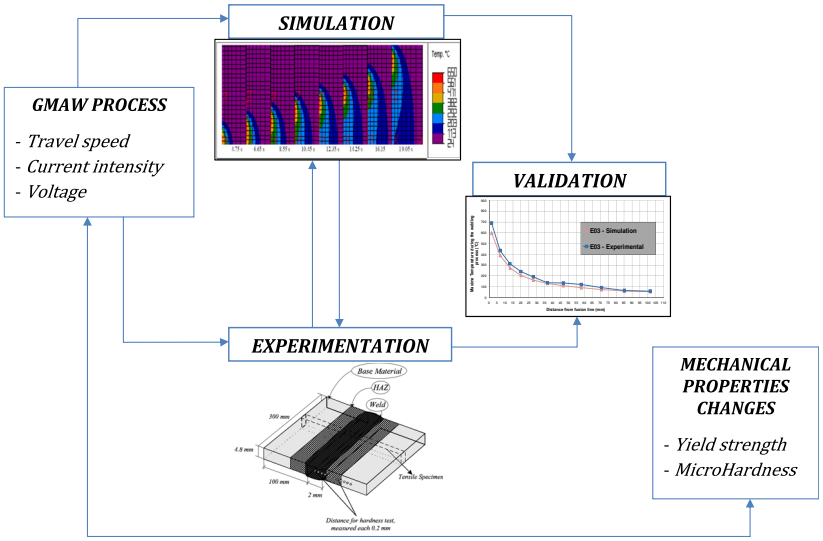

Fig. 1. Flow diagram of the research process.

Table 4
Results for two different temperatures.

	For room temperature (35 °C)	For high temperature (652 °C)
Gr	9.66×10^6	1.73×10^8
Nu – Upper plate	27.56	64.67
Nu – Lower plate	13.78	28.18
h – Upper plate	3.76 W/m^2 °C	11.83 W/m^2 °C
h – Lower plate	1.88 W/m^2 °C	5.16 W/m^2 °C

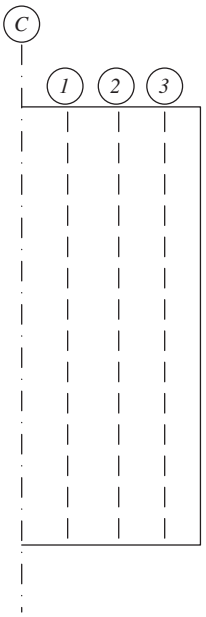

Fig. 2. Refined mesh with seven nodes-symmetric representation of a welded plate (only four nodes because of the symmetry about central node C).

for heat transfer coefficient were computed. For the upper plate h_m is 5.374 W/m^2 °C and for the lower plate h_m is 2.536 W/m^2 °C. The mesh of FE model [20] was constructed with 600 rectangular elements. The mesh is thinner near to the cord in order to capture the variation in the hottest zone. A Gaussian distribution was selected because this represents a close approximation to the distribution of heat flux [16]. A length equal to twice the width of the weld cord (15 mm) was covered. The mess was refined to get seven nodes for the given length as shown in Fig. 2. The generating function that represents the unit distribution is:

$$f = \frac{1}{\sqrt{2\pi}} e^{\left[-\left(\frac{x}{10}\right)^2\right]} \tag{5}$$

The x variable is the distance to the central node, in millimeters. The net heat was calculated using the following equation

$$Q_{NET} = \eta \cdot Q_{TOTAL} = \eta \cdot I \cdot V \tag{6}$$

where η is the heat efficiency of the arc.

Table 5 shows the thermal nodal load for each one of the welding experiments.

Table 7
Properties of the base material before the welding process.

Material	Yield strength, S_y (MPa)	Ultimate strength, S_u (MPa)	Elongation (%)	Microhardness (HV)
AA 6061-T6	286	318	5.44	106

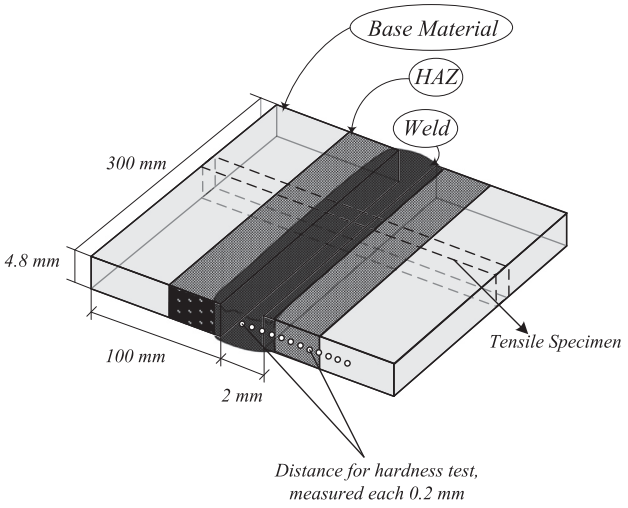

Fig. 3. Welded plates with dimensions and the representation of a tensile specimen.

Table 5
Process conditions, nodal loads and times for each welding experiment.

Welding experiment	I (Amp)	v (Volt)	Vel. (mm/s)	Q_{NET} (J/s)	Dt (s)*	$N_{CENTRAL}$	N_1	N_2	N_3
E01	120	18	5.26	1728	1.6667	246.15	190.77	92.31	25.85
E02	120	20.1	4.34	1920	1.6667	273.50	211.97	102.56	28.72
E03	120	18	6.6	1728	0.8333	246.15	190.77	92.31	25.85
E04	120	19.6	6.4	1920	0.8333	273.50	211.97	102.56	28.72
E05	140	17.7	6.7	2016	0.8333	287.18	222.56	107.69	30.15
E06	140	21.2	7.32	2240	0.8333	319.09	247.29	119.66	33.50
E07	140	20.5	5.36	2240	1.0000	319.09	247.29	119.66	33.50
E08	140	23.5	5.45	2688	1.0000	382.91	296.75	143.59	40.21

Note: Nodal loads have a symmetry with respect to the central node.
* Dt is the interval of time it takes to change the load from one node to another.

Table 6
Chemical composition of the materials (wt.%).

Material	Al	Si	Fe	Cu	Mn	Mg	Cr	Ti	Zn	Sn
AA 6061-T6	97.782	0.7822	0.2395	0.1167	0.0159	1.0977	0.0015	0.0138	0.003	0.0012
AWS ER4043	94.540	4.8	0.24	0.17	0.05	0.05	0.05	0.05	0.05	–

3. Materials and methods

Plates of commercial AA6061-T6 alloy with dimensions of 300 mm × 100 mm × 4.8 mm were used in this study and a filler wire ER4043, 1.19 mm in diameter, was employed. The chemical composition of both materials is provided in Table 6 and the mechanical properties of the base material in Table 7. To evaluate the change in the mechanical properties of the 6061-T6 aluminum alloy, the yield strength and microhardness before and after the welding process were measured. The results of the model were validated by experiments that measure the temperature transverse to the heat source in different zones. The data to validate the model

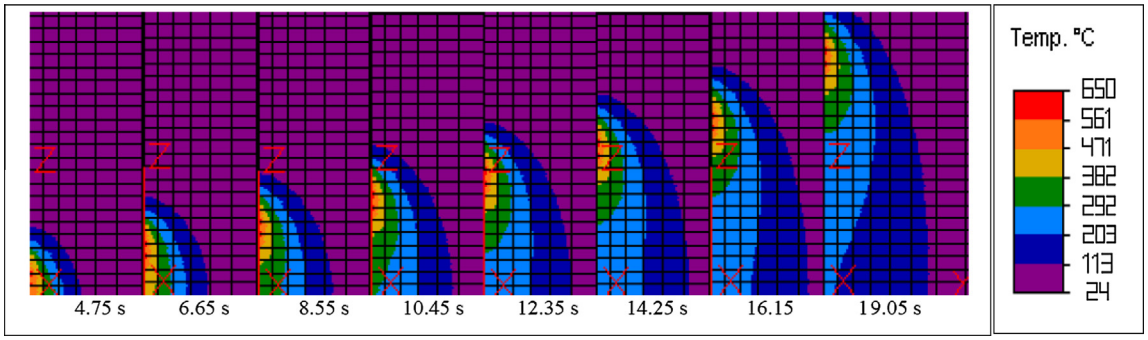

Fig. 4. Different stages in the formation and stabilization of the temperature field for E01 (120 A, 18 V and 5.26 mm/s).

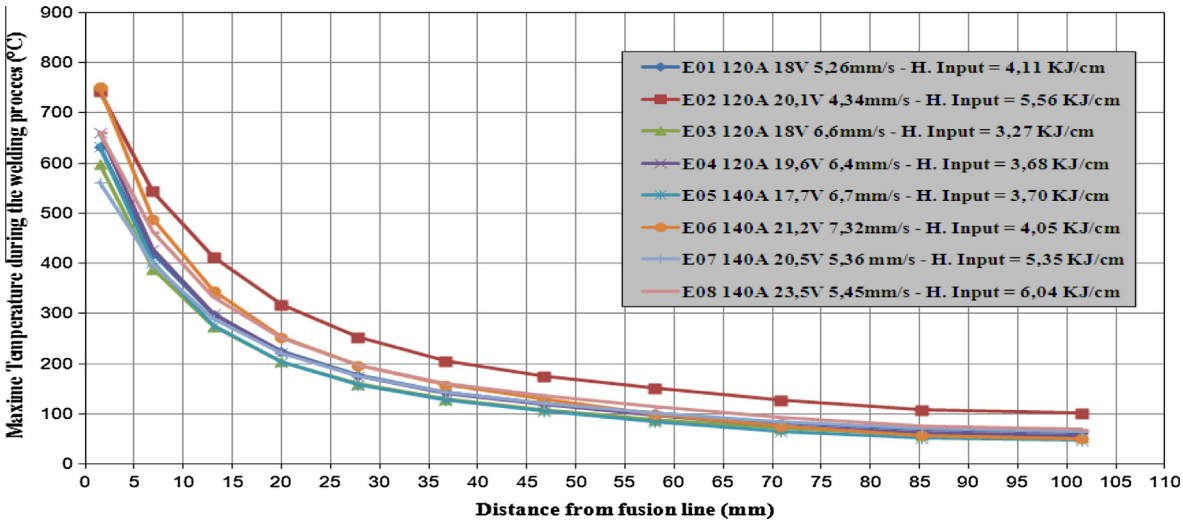

Fig. 5. Peak temperatures obtained by the finite element numerical solution in the middle of plate, using the parameters of welding.

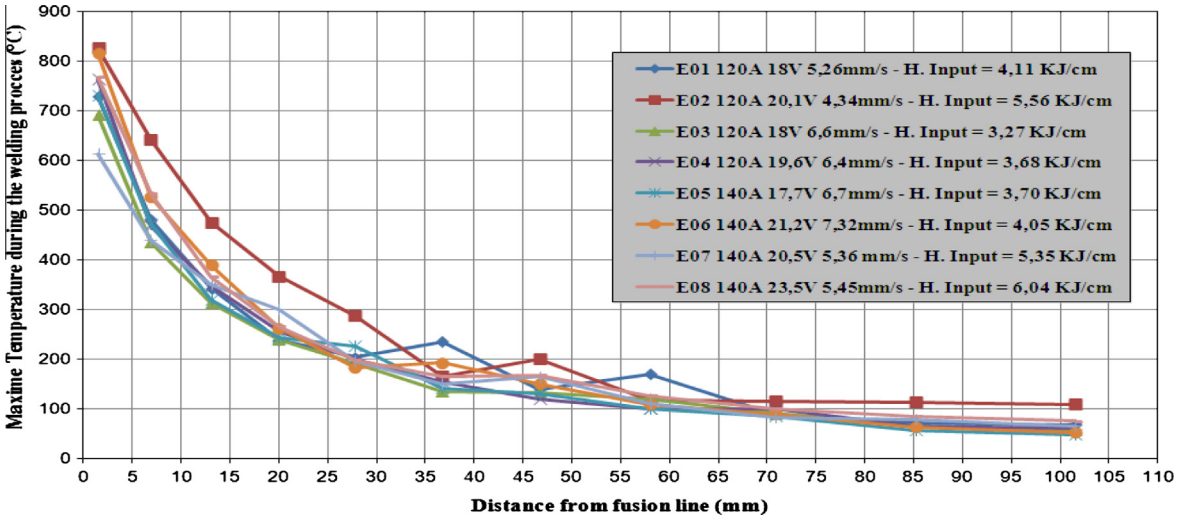

Fig. 6. Peak temperatures obtained experimentally with the same conditions.

were obtained by measuring the temperature of welded sheets using contact thermocouples. Thermocouples were placed on a line perpendicular to the weld, to cover a distance equal to the width of the heat affected zone. The thermocouples were chromel–constatan type E Class 1, with a measurement range from 40 °C to 900 °C; its error limit was ±1.5 °C and ±0.4% limit extension cord with a standard error of 1.5 °C. Alloy sheets of AA6061T6 4.8 mm thick were welded with AWS-ER-4043 used as the filler. To perform the welding, the Lincoln Power MIG 350 machine was used, and the following welding process parameters were studied: current intensity, arc voltage, wire speed output, shielding gas flow, and travel speed of the torch.

The hardness curves were taken from sections of fractured tensile test specimens, taking a line perpendicular to the weld axis as an abscissa. The distance was taken from the center of the weld, moving away from it, as shown in Fig. 3 that is also illustrating the specimens (transversal view) used for the tensile test. Everything was according to the ASTM: E8/E8 M–11 Standard, in a universal testing machine Shimadzu UHM 50 TV model. According to the ASTM: E384–11$^{\varepsilon 1}$ the microhardness profiles were generated, applying a 100 g (0.981 N) load with a Vickers indent for 10 s. The Vickers microdurometer with automatic load Shimadzu brand 160 Rodi model was employed.

4. Results and discussion

Fig. 4 shows the evolution in the temperature field until it takes on quasi-stationary shape. When the temperature field is not affected by the plate edges the temperatures remain constant for a coordinated system moving at the same speed and in the same direction as the heat source. This means that thermal cycles experienced by points at the same distance from the weld axis were identical, so the resulting mechanical properties should also be the same. The size of the stable area is smaller as the heat input increases or the size of the plate is reduced. Obtaining the maximum temperature at any point on the plate during the application of the

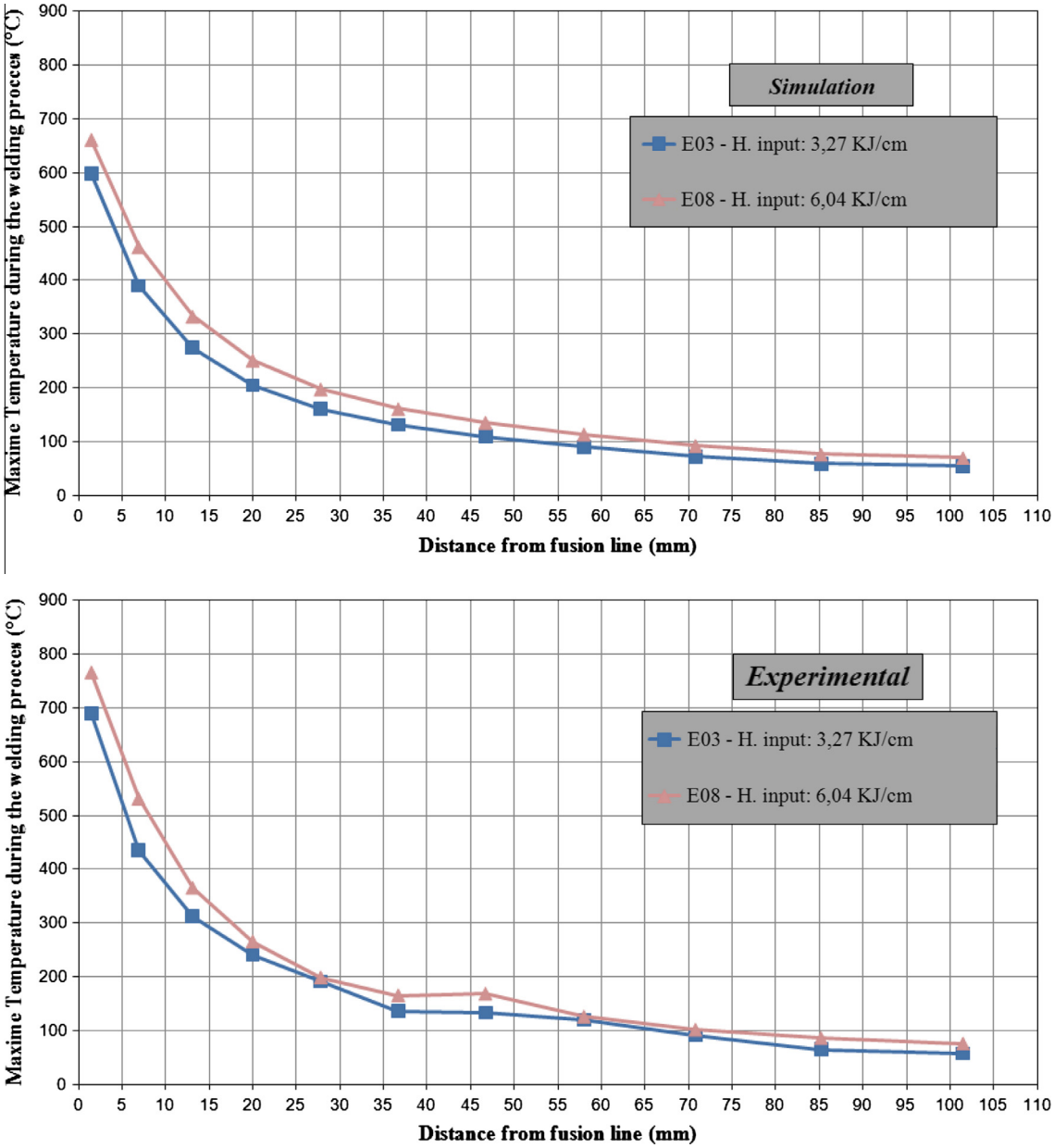

Fig. 7. Differences in temperature between a high heat input and a low heat input simulation and experimental exercise.

welding thermal cycle is important to determine the microstructural changes occurring at that position. According to [2] the points where the maximum and minimum hardness occur are related to these temperatures. Fig. 5 illustrates the temperature curves obtained by the numerical solution, and Fig. 6 shows the experimental data, in its legend is shown every experiment and process conditions, for current, voltage, travel speed and heat input. Simulation results and experimental data showed good agreement as Fig. 7 illustrated. The maximum temperature difference is observed in the 0–5 mm zone; due to the material fusion that is not considered in the FE model. It is possible to verify that a very high temperature gradient (up to 40 °C/mm) exists in the area from 0 to 15 mm and that a reduction of the slope occurs moving away from the center of the weld to reach a value of 0.25 °C/mm near the edge. The temperature value is closely related to the heat input, with lower heat input then lower temperatures are obtained as can be appreciated in Fig. 7, this is valid for simulation results and experimental data.

On the other hand, the main change in the process conditions is the current intensity (Figs. 5 and 6); therefore one experiment at 120 A and one at 140 A were selected. Before the welding process the yield strength (Sy) was 286 MPa and the Vickers microhardness was 106 HV (Table 7). Two main experiments with different input values for current, voltage and travel speed are analyzed to calculate the maximum reduction in these mechanical properties.

4.1. Experiment 1

4.1.1. Process conditions: 120 A; 18.0 V; 5.26 mm/s corresponding to an input heat of 4.11 KJ/cm

The yield strength was determined after the welding process for every plate and a Vickers microhardness profile was generated; this profile for experiment 01 is shown in Fig. 8. With these conditions the minimum value of microhardness and yield strength were:

$$(S_y)_{\text{after}} = 157.1\text{MPa}$$
$$\text{Hardness}_{\text{after}} = 58.1HV$$

Then,

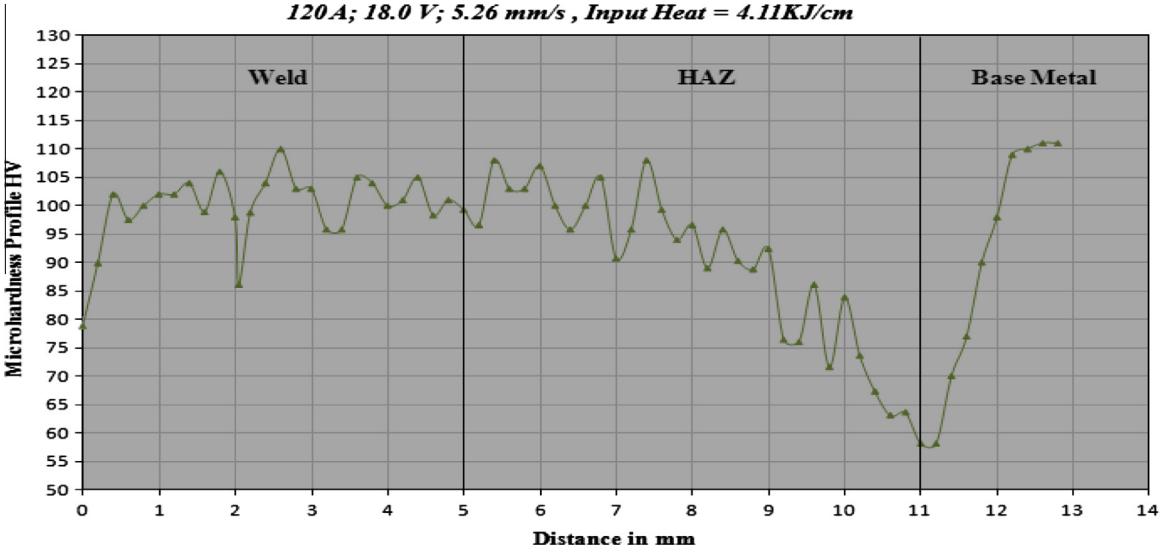

Fig. 8. Transverse microhardness profile in as-welded experiment 01.

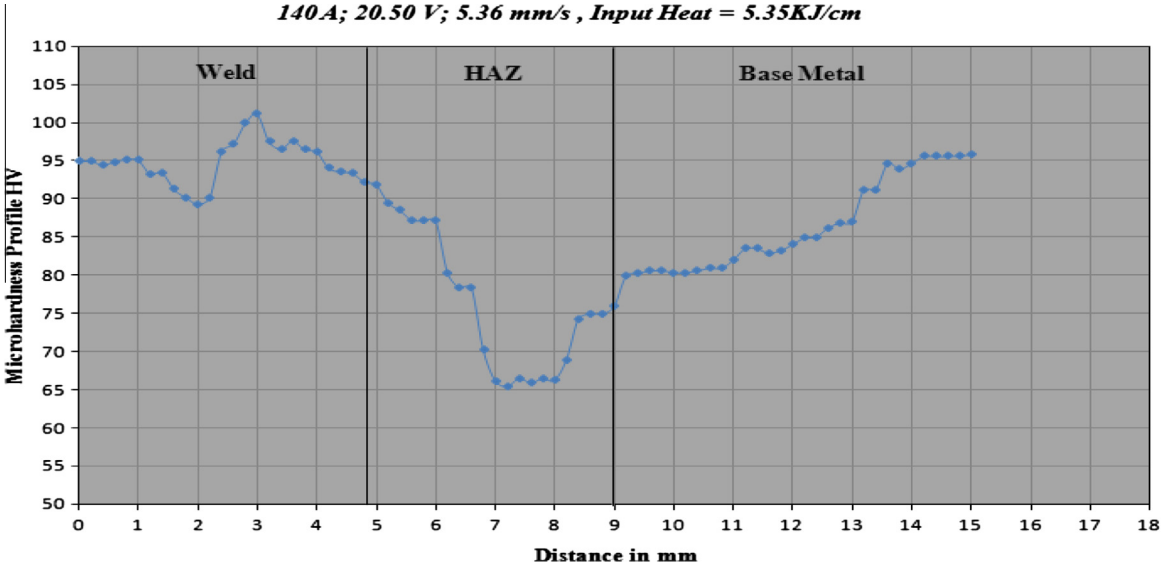

Fig. 9. Transverse microhardness profile in as-welded experiment 07.

$$\%_{\text{reduction-stress}} = \frac{S_y - (S_y)_{\text{after}}}{S_y} \cdot 100\% = \frac{286\text{MPa} - 157.1\text{MPa}}{286\text{MPa}} \cdot 100\% = \frac{128.9\,\cancel{\text{MPa}}}{286\,\cancel{\text{MPa}}} \cdot 100\% = \underline{45.1\%}$$

$$\%_{\text{reduction-hardness}} = \frac{\text{Hardness}_0 - \text{Hardness}_{\text{after}}}{\text{Hardness}_0} \cdot 100\% = \frac{106HV - 58.1HV}{106HV} \cdot 100\% = \underline{45.2\%}$$

4.2. Experiment 7

4.2.1. Process conditions: 140 A; 20.5 V; 5.36 mm/s corresponding to an input heat of 5.35 KJ/cm.

The yield strength was determined after the welding process for every plate and also a Vickers microhardness profile was generated, this profile for experiment 07 is shown in Fig. 9. With these conditions the minimum value of microhardness and yield strength were:

$$(S_y)_{\text{after}} = 169\ \text{MPa}$$
$$HV_{\text{after}} = 65.4$$

Then,

$$\%_{\text{reduction-stress}} = \frac{S_y - (S_y)_{\text{after}}}{S_y} \cdot 100\% = \frac{286\text{MPa} - 169\text{MPa}}{286\text{MPa}} \cdot 100\% = \frac{117\,\cancel{\text{MPa}}}{286\,\cancel{\text{MPa}}} \cdot 100\% = \underline{40.9\%}$$

$$\%_{\text{reduction-hardness}} = \frac{\text{Hardness}_0 - \text{Hardness}_{\text{after}}}{\text{Hardness}_0} \cdot 100\% = \frac{106HV - 65.4HV}{106HV} \cdot 100\% = \underline{38.4\%}$$

The changes in these mechanical properties are similar and confirm the correlation between the yield strength and the hardness of the alloy, because the reduction percentage was calculated for different experiments with different process conditions and the values were very close in magnitude. According to the TEM analysis for the alloy, before and after welding, is possible to affirm that the changes on the mechanical properties were caused by the evolution of precipitates due to the effect of welding heat input [21]; as can be appreciated in Fig. 10. These TEM photographs show the sequence of formation and dissolution of the precipitates β'', β' and β and the formation of Mg_2Si. This agrees with the conclusions obtained for [1,2,5,10].

Fig. 11 shows a thermogram in the heat affected zone (HAZ) for experiment 07 (H. input = 5.35 KJ/cm), the reduction on the mechanical properties is due to the transformation of β'' precipitate in β' precipitate. It is β'' phase, the main factor in the strengthening of the alloy due to its needle shape and distribution. The temperature ranges for the different precipitates are [2].

GP: 90–150 °C
β'': 160–240 °C
β': 240–380 °C
β: 380–480 °C

For this experiment, the temperature range for β' phase is 283–360 °C as illustrated in Fig. 11, showing good agreement with values reported in the literature [2]. Fig. 6 shows that temperature in the heat affected zone (HAZ) is above the formation temperature for β' (and also above dissolution temperature for β'', 250 °C) which explains the reduction on the mechanical properties. The precipitation sequence for this alloy is [2,22].

$$\alpha' \rightarrow \alpha + GP \rightarrow \alpha + \beta'' \rightarrow \alpha + \beta' \rightarrow \alpha + \beta$$

where α: solid solution, α': supersaturated solid solution.

According to the thermogram shown in Fig. 11 the precipitation sequence and corresponding formation–dissolution temperatures are:

GP: formation 146 °C
β'': dissolution 250 °C
β': formation 283 °C–dissolution 360 °C
β: formation 479 °C

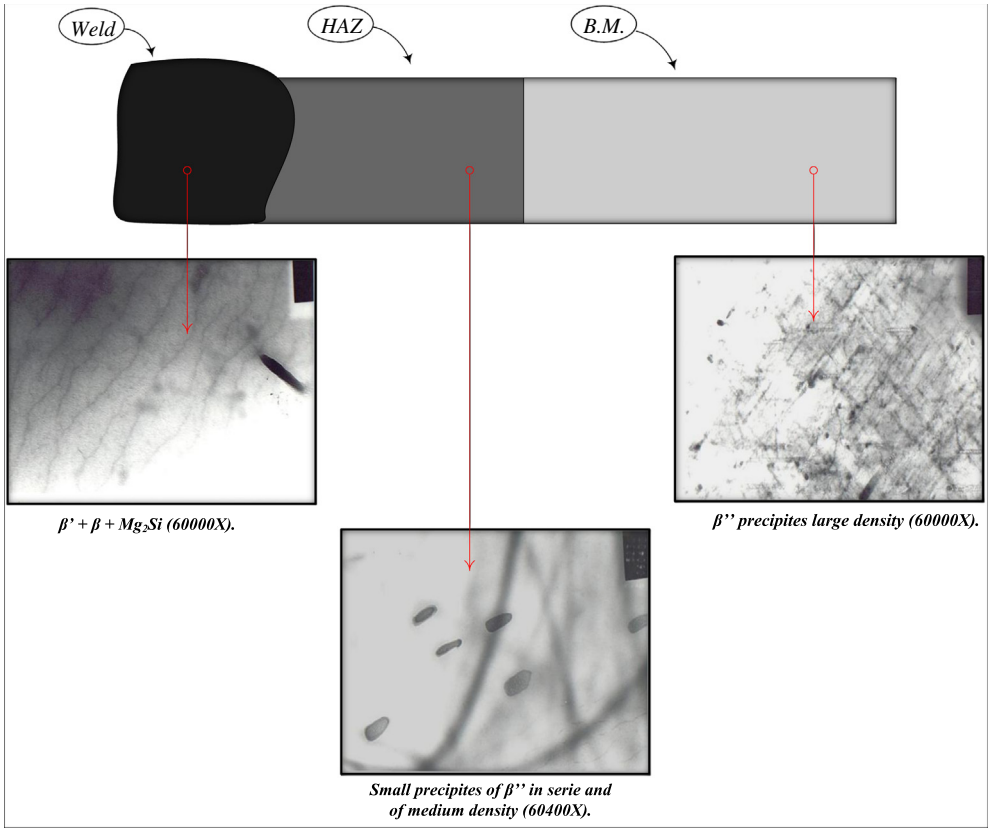

Fig. 10. Micro and nanoestructural in the weld, HAZ and base metal.

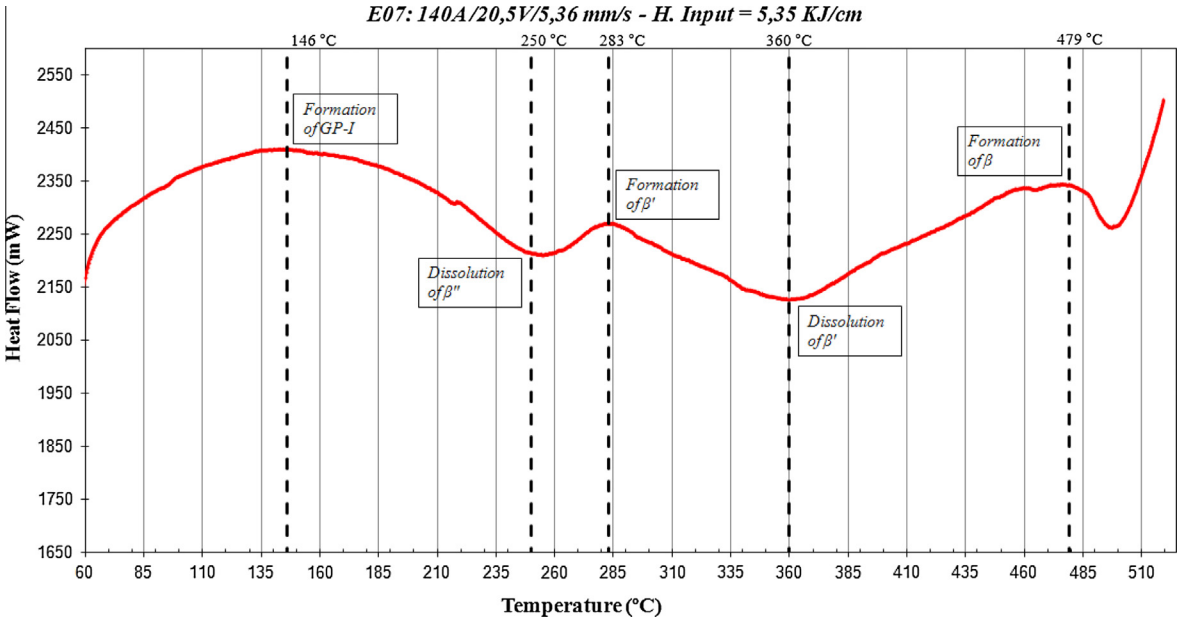

Fig. 11. Thermogram for the material at the minimum hardness zone.

The precipitation sequence and formation–dissolution temperatures agree with values reported in the literature.

5. Conclusions

The transient thermal analysis using FEM to model welded joints has produced reasonably accurate results: the error between the model and the experimental results state in the order of 8%. Integration of numerical and experimental results makes it possible to obtain an excellent correlation between the temperatures reached, Vickers microhardness, yield strength and microstructural changes in different heat-affected zones. Mechanical behavior after welding is strongly influenced by heat input into the base material, establishing different zones, where are particularly interesting the heat affected zone that present an extreme minimum in hardness. This minimum hardness zone corresponds with the failure zone in tensile test (6–8 mm from the center of the weld). The range of reduction on the mechanical properties, based on yield strength and microhardness, is 38–45%. This reduction is due to the dissolution of β'' and the formation of β'. The methodology and results of this work could be used as a tool to optimized welding processes based on the prediction of mechanical properties such as yield strength and microhardness. The use of computational modeling reduces the number of experiments and therefore the cost.

Future experimental work in this area should aim e.g. the effect of a heat treatment on the aging of precipitation hardening post-welding (PWHT) for Al-6061 alloys, to quantify the variation on the mechanical properties based on the yield strength and microhardness for as-welded and post-welded joints.

Acknowledgments

The authors wish to express their gratitude to *Aluminio Reynolds Santo Domingo Inc.* for donating the material utilized in this investigation and to the Mechanical and Materials Engineering department from the *Universidad Politécnica de Valencia* (*Spain*) for their support in the Differential Scanning Calorimetry (DSC) and Transmission Electron Microscopy (TEM) laboratories.

References

[1] Mayazaki H, Nisio K, Katoh M, Mukae S, Kerr W. Quantitive investigation of heat – affected zone cracking in aluminum alloy A 6061. Weld J 1990;69:362–71.
[2] Malin V. Study of metallurgical phenomena in the HAZ of 6061 - T6 aluminum welded joints. Weld Res Supl 1995;315.
[3] Torres J. Evolución microestructural de la aleación de aluminio 6061 durante el proceso de soldadura MIG. Ingeniería desarrollo, 12. Universidad del Norte; 2002.
[4] Miyazaki M, Miyauchi H, Yugiyama Y, Shinoda T. Puckering phenomenon and its prevention in GMAW welding of aluminum alloys. Weld J 1994.
[5] Akio H, Hirotaka T, Hiroto Y, Nobutaka K, Kojiro K. Quantitative evaluation of softened regions in weld heat-affected zones of 6061–T6 aluminum alloy—characterizing of the laser beam welding process. Metall Mater Trans 1999;30:2115–20.
[6] Liu C, Yi X. Residual stress measurement on AA6061-T6 aluminum alloy friction stir butt welds using contour method. Mater Des 2013;46:366–71.
[7] Riahi M, Nazari H. Analysis of transient temperature and residual thermal stresses in friction stir welding of aluminum alloy 6061–T6 via numerical simulation. Int J Adv Manuf Technol 2011;55(1–4):143–52.
[8] Myhr OR, Grong Ø, Fjær HG, Marioara CD. Modelling of the microstructure and strength evolution in Al–Mg–Si alloys during multistage thermal processing. Acta Mater 2004;52(17):4997–5008.
[9] Ambriz RR, Barrera G, García R, López VH. A comparative study of the mechanical properties of 6061–T6 GMA welds obtained by the indirect electric arc (IEA) and the modified indirect electric arc (MIEA). Mater Des 2009;30(7):2446–53.
[10] Ambriz RR, Barrera G, García R, López VH. The microstructure and mechanical strength of Al-6061-T6 GMA welds obtained with the modified indirect electric arc joint. Mater Des 2010;31(6):2978–86.
[11] Ambriz RR, Chicot D, Benseddiq N, Mesmacque G, de la Torre SD. Local mechanical properties of the 6061–T6 aluminum weld using micro-traction and instrumented indentation. Eur J Mech – A Solids 2011;30(3):307–15.
[12] Florea RS, Bammann DJ, Yeldell A, Solanki KN, Hammi Y. Welding parameters influence on fatigue life and microstructure in resistance spot welding of 6061–T6 aluminum alloy. Mater Des 2013;45:456–65.
[13] Dong P, Li H, Sun D, Gong W, Liu J. Effects of welding speed on the microstructure and hardness in friction stir welding joints of 6005A–T6 aluminum alloy. Mater Des 2013;45:524–31.
[14] Patil HS, Soman SN. Effect of weld parameter on mechanical and metallurgical properties of dissimilar joints AA6082–AA6061 in T6 condition produced by FSW. Fract Struct Integrity 2013;0(24):151–60.
[15] Maisonnette D, Suery M, Nelias D, Chaudet P, Epicier T. Effects of heat treatments on the microstructure and mechanical properties of a 6061 aluminum alloy. Mater Sci Eng: A 2011;528(6):2718–24.
[16] Moore JE, Bibby MJ, Goldak JK. A comparison of the pint source and Finite Elements Schemes for computing weld cooling, In: Proceedings of the JDC university research symposium, ASM; 1985, pp. 1–9.
[17] Totten GE, MacKenzie DS, editors. Handbook of aluminum. Alloy production and materials manufacturing, vol. 2. CRC Press; 2003.

[18] Ozisik M. Transferencia de Calor. McGraw-Hill; 1979.
[19] Cengel Y, Ghajar A. Heat and mass transfer: fundamentals and applications + EES DVD for heat and mass transfer. 4th ed. McGraw-Hill Science/Engineering/Math; 2010.
[20] Reddy JN, Gartling DK. The finite element method in heat transfer and fluid dynamics. 2nd ed. CRC Press; 2000.
[21] Song M. Modeling the hardness and yield strength evolutions of aluminum alloy with rod/needle-shaped precipitates. Mater Sci Eng: A 2007;443(1–2):172–7.
[22] Edwards GA, Stiller K, Dunlop GL, Couper MJ. The precipitation sequence in Al–Mg–Si alloys. Acta Mater 1998;46(11):3893–904.